International Journal of Heat and Mass Transfer 52 (2009) 56–66

Contents lists available at ScienceDirect

International Journal of Heat and Mass Transfer

journal homepage: www.elsevier.com/locate/ijhmt

A numerical study of unsteady natural convection induced by iso-flux surface cooling in a reservoir model

Tomasz P. Bednarz *, Chengwang Lei, John C. Patterson

School of Engineering, James Cook University, Townsville, Qld 4811, Australia

ARTICLE INFO

Article history:
Received 26 March 2008
Received in revised form 23 June 2008
Available online 25 August 2008

Keywords:
Unsteady natural convection
Reservoir
Convective instability
Numerical simulations

ABSTRACT

Unsteady natural convection in a reservoir model subject to constant cooling at the water surface is considered in this paper. In such a case, the unequal heat loss resulting from a varying water depth creates a horizontal temperature gradient which in turn drives a horizontal exchange flow between the coastal region and the main water body of the reservoir. Understanding of the flow mechanisms pertinent to this flow is important for predicting the transport of nutrients and pollutants across the reservoir.

The present numerical simulations impose random perturbations at the water surface in order to trigger flow instabilities. First, numerical tests are carried out to investigate the flow response to different perturbation amplitudes. These tests reveal a linear range of the flow response to the perturbations. Subsequently, the transient flow development at different stages is described in details based on numerical data, and the effects of the Grashof number on the unsteady flow are examined.

1. Introduction

Diurnal heating and cooling of the sidearms of lakes and reservoirs with gently sloping bottoms may result in large scale convective circulations. Typically the input of solar radiation through the water surface in the day-time results in relatively warm shallow regions. The absorption of solar radiation decreases with the water depth, and thus a stable stratification is established in the water body. In shallow waters, the water depth is smaller than the penetration depth of solar radiation, and the radiation reaches the bottom where the residual radiation is absorbed and then re-emitted into the water layer above the bottom. This bottom heating works as a destabilizing mechanism, which competes with the stable stratification. Conversely, night-time cooling through the water surface results in relatively cool shallow regions and distinct near-shore horizontal temperature gradients because the shallow regions cool relatively faster than deeper regions. As a result, a cold water undercurrent is created which proceeds toward the deeper regions along the bottom. At the same time, cooling at the water surface may generate instabilities in the form of plunging thermals originating from the surface. In natural systems, all the above-mentioned mechanisms work together in a complex way over diurnal cycles. The convective motions generated in these ways influence the transport of nutrients and pollutants or dissolved constituents between the near-shore and central regions of the water body, and thus may play a central role in determining the water quality, along with a range of other processes. A broad review of dynamical processes pertinent to lakes and reservoirs can be found in Imberger and Patterson [1].

In recent years, the convective transport mechanisms arising from these diurnal heating and cooling cycles have attracted significant attention from researchers, and many reports on topics of horizontal exchange flows can be found in the literature [2–6]. However, previous investigations are limited in general to simple geometries such as a triangular cavity, which is a poor representation of real systems, although the triangular cavity is a good starting point for further investigations.

Horsch and Stefan [7] and Horsch et al. [8] studied numerically and experimentally the night-time cooling phase in a triangular cavity with a constant heat flux at the top surface. They found that the flow in the initial stage consisted of a number of re-circulating regions associated with sinking cold-water plumes. At the same time, they observed a gravity current of cold water emerging from the tip region and flowing downwards along the sloping bottom. After a sufficient period of time, the gravity current (undercurrent) travelled the full length of the domain to create a cell-like convective circulation in the entire cavity. The effect of topography with a decreasing water depth on the distribution of an originally uniform incoming heat flux was reported by Adams and Wells [9] and Monismith et al. [10], based on their field observations. They were able to measure the velocities associated with the surface outflow of warm water from the edges of reservoir sidearms, which were of the order of 5 cm/s. Their observations are consistent with the recent numerical simulations of flow responses to periodic heating and cooling by Lei and Patterson [11], which generally showed a time lag in the overall flow response when the thermal forcing is switched between heating and cooling. The analyses carried out

* Corresponding author. Tel.: +61 7 4781 5218; fax: +61 7 4781 6788.
E-mail address: tomasz.bednarz@jcu.edu.au (T.P. Bednarz).

0017-9310/$ - see front matter © 2008 Elsevier Ltd. All rights reserved.
doi:10.1016/j.ijheatmasstransfer.2008.06.029

Nomenclature

A	aspect ratio, $A = H/L$
A_s	bottom slope, $A_s = H/L_s$
C_p	specific heat (J/kg K)
g	acceleration due to gravity (m/s^2)
Gr	Grashof number, $Gr = g\beta H_0 H^4/(\nu^2 k)$
H	maximum water depth (m)
H_0	volumetric cooling intensity at the surface (mK/s), $H_0 = I_0/(\rho_0 C_p)$
I_0	rate of heat loss at water surface (W/m^2)
k	thermal diffusivity (m^2/s)
L	length of the model (m)
L_s	horizontal length of the slope (m)
n	coordinate normal to the bottom (m)
p	pressure (N/m^2)
Pr	Prandtl number, $Pr = \nu/k$
Ra	Rayleigh number, $Ra = GrPr$
Ra_L	local Rayleigh number
Q, Q_m	exchange flow rates
t	time (s)
t_B	onset time of instabilities (s)
T	temperature (K)
T_0	reference temperature (K)
$\vec{u}$	velocity (m/s)
u and v	velocity components in x and y directions (m/s)
x and y	coordinates in horizontal and vertical directions (m)

Greek symbols

β	coefficient of thermal expansion (1/K)
ε	intensity of perturbations
λ	thermal conductivity (W/mK)
ν	kinematic viscosity (m^2/s)
ρ_0	density (kg/m^3)
τ_{dev}	standard deviation of the temperature

by Farrow and Patterson [12], Farrow [13] and, Lei and Patterson [11] revealed that, during both the cooling and heating phases, thermal instabilities break the residual circulation and reverse the flow in deep waters. Lei and Patterson [2] also considered the convective circulations in a triangular geometry generated by surface cooling, and presented a scaling analysis revealing three laminar flow regimes, namely conductive, transitional and convective regimes, depending on the Rayleigh number. Their numerical simulations verified their scaling predictions. Earlier the same authors [3,4] also studied the effect of day-time heating-induced natural convection in a shallow wedge.

As mentioned above, all of the reviewed works, except those in [6,11], were confined to a triangular cavity, which is a poor geometric representation of real systems. The present numerical investigation extends those works with the addition of an adjacent region of uniform water depth, which, despite still being a significant simplification of real systems, is a more realistic model than a simple triangular cavity. The cooling case is reinvestigated in this model. In the following, the methodology of triggering initial flow instabilities is presented; numerical results describing the flow development are described in detail; and a scaling prediction of the onset time of instability is derived.

2. Numerical model

Fig. 1 shows a two-dimensional (2D) reservoir model consisting of two distinct regions: one with a sloping bottom and the other with a uniform water depth. The dimensions of the numerical model are chosen to correspond to those of a laboratory reservoir model. The total length of the model is $L = 2$ m with a maximum water depth of $H = 0.1$ m and a slope inclination of $A = 0.1$. A Cartesian coordinate system is adopted with the origin located at the tip of the reservoir model (see Fig. 1). Previous investigations showed that 2D numerical simulations can reproduce the major flow features despite the three-dimensional (3D) nature of the flow with the presence of flow instabilities [2].

The flow and temperature fields in the reservoir model are governed by equations of continuity (1), momentum (2), and energy (3) given below:

$$\nabla \cdot \vec{u} = 0 \tag{1}$$

$$\frac{D\vec{u}}{Dt} = -\frac{1}{\rho_0}\nabla p + \nu\nabla^2\vec{u} + g\beta(T - T_0)\begin{bmatrix}0\\1\end{bmatrix} \tag{2}$$

$$\frac{DT}{Dt} = k\nabla^2 T \tag{3}$$

where $\vec{u}$ is the fluid velocity vector, t is the time, p is the pressure, T is the temperature, ρ_0 is the density at the reference temperature T_0, k is the thermal diffusivity, g is the gravitational acceleration, β is the thermal expansion coefficient, and ν is the kinematic viscosity.

The boundary conditions are defined as follows:

- On the sloping and horizontal bottoms, rigid non-slip wall boundary conditions apply ($\vec{u} = 0$). These walls are also thermally insulated ($\partial T/\partial n = 0$, where n is the direction normal to the wall).
- The deep-end vertical wall is also adiabatic ($\partial T/\partial x = 0$), rigid, and non-slip ($\vec{u} = 0$).
- The tip is cut off at $x = 0.016$ m in order to avoid a singularity, and an extra rigid non-slip ($\vec{u} = 0$) and adiabatic ($\partial T/\partial x = 0$) boundary is assumed there.
- The water surface is assumed to be stress free ($v = 0$ and $\partial u/\partial y = 0$, where u and v denote, respectively, the horizontal and vertical components of the velocity). The thermal boundary condition at the water surface is given by:

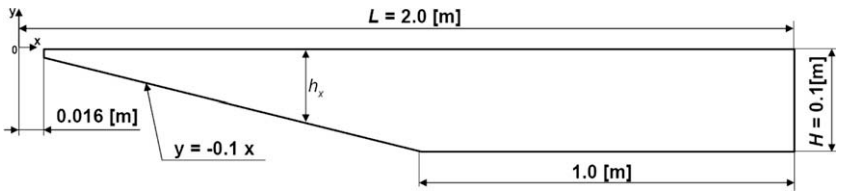

Fig. 1. Schematic of the considered reservoir model.

$$\frac{\partial T}{\partial y} = -\frac{H_0}{k} + \varepsilon \cdot [\text{random}(0,1) - 0.5] \cdot \frac{H_0}{k} \tag{4}$$

In the above equation, the quantity H_0 is given by $H_0 = I_0/(\rho_0 C_p)$, where I_0 is the rate of heat loss per unit surface area, and C_p is the specific heat evaluated at the reference temperature T_0. The second term on the right-hand side of Eq. (4) represents a random heat flux perturbation at the water surface, with ε specifying the intensity of perturbations, and random(0,1) generating a random number between 0 and 1 [14]. The perturbations to the surface boundary condition are necessary for the investigation of the onset of plunging surface plumes, as discussed below.

At the initial state the fluid is stationary ($\vec{u} = 0$) with a uniform temperature of $T_0 = 293.15$ K across the whole computational domain.

The present work is concerned with unsteady natural convection in the reservoir model. For easier characterization of such flows, four non-dimensional parameters are used herein (Prandtl number, Grashof number, the aspect ratio, and the bottom slope). They represent the important properties of the fluid, the thermal forcing, and the geometry. The first parameter (Prandtl number) describes the relative strength of the diffusion of momentum to that of heat:

$$Pr = \frac{v}{k}. \tag{5}$$

The second parameter (Grashof number) expresses the ratio of buoyancy forces to viscous forces and is defined as follows:

$$Gr = \frac{g\beta H_0 H^4}{v^2 k} = \frac{Ra}{Pr}, \tag{6}$$

where Ra is the Rayleigh number. The third parameter denotes the aspect ratio which defines the geometry of the cavity:

$$A = \frac{H}{L} = 0.05. \tag{7}$$

and the last parameter is the bottom slope which characterizes the inclination of the slope:

$$A_s = \frac{H}{L_s} = 0.1. \tag{8}$$

For our computed cases with water as the medium, the Prandtl number takes a constant value of $Pr = 7.07$; and A and A_s are both constant for all computations. The numerical simulations are therefore carried out for different Grashof numbers ($Gr = 10^4$, 10^5, 10^6, 10^7, and 5×10^7) in order to examine how the flow responds to different strengths of surface cooling.

To describe the horizontal exchange flow across a vertical sectional plane at a given x location, a (two-dimensional) volumetric flow rate $Q(x)$ is defined as [2,8]

$$Q(x) = \frac{1}{2}\int_{-h_x}^{0} |u| \mathrm{d}y, \tag{9}$$

where h_x is the local water depth. An averaged volumetric flow rate Q_m is obtained by integrating $Q(x)$ along the horizontal x-direction as follows:

$$Q_m = \frac{1}{L}\int_0^L Q(x)\mathrm{d}x \tag{10}$$

Eqs. (1)–(3) are numerically solved using a finite volume method [15]. A second-order time-accurate formulation is employed in all subsequent computations, and the pressure–velocity coupling is carried out using the SIMPLE method [15,16] with the convective term discretised using a second-order upwind scheme and the diffusion term discretised using a second-order central-differenced scheme. A non-uniform grid system is constructed with finer grids distributed in the vicinity of all the wall boundaries, close to the tip region and in the region where the slope finishes. The number of nodes was chosen to be 861×51 after a grid-dependency test was carried out (described in Section 4). Additionally, the working fluid (water) is assumed to be incompressible and Newtonian, and the Boussinesq approximation is employed in the present modeling. All results reported in this paper are performed using a double precision solver.

3. Random perturbation tests

The specification of surface cooling suggests that the configuration is potentially unstable in a Rayleigh–Benard sense. To trigger an instability a perturbation to a base flow state is required. In general, numerical experiments require a small random perturbation to be applied to the base flow to ensure a random production of instabilities, and a common method of introducing this is to apply small perturbations to one of the boundary conditions [17,18]. In this case, the perturbation was applied to the surface heat flux, as specified in Eq. (4) above. The response of the system to different amplitudes of the heat flux perturbation applied at the water surface is examined. Computations are carried out for $Pr = 7.07$, $Gr = 10^7$, and $\varepsilon = 0.5\%$, 1.0%, 1.5%, 2.0%, 3.0%, and 4.0%, respectively. The test is concerned with the initial stage of the flow development only, in which instabilities take place.

The system response to the perturbations is well represented by time series of the standard deviation of the temperature taken directly from the area below the water surface at $y = -0.001$ m. However, only temperatures in the deep-water region (for $x > 1.0$ m) are included in the calculation of the standard deviation due to the strong conduction effect in the area close to the tip.

Fig. 2a shows the horizontal temperature profiles taken below the water surface ($y = -0.001$ m) for three sample perturbation amplitudes ($\varepsilon = 0.5\%$, 2%, and 4%, respectively) and at $t = 130$ s when the instabilities are well-established. It can be clearly seen in Fig. 2a that the temperature profiles show clear wave-like characteristics and some irregularities, and the temperature profiles obtained with different perturbation amplitudes follow the same pattern. Also it can be observed that different perturbation strengths result in different amplitudes of the temperature responses. In Fig. 2a, all the temperature profiles are plotted for the range of $x \geqslant 0.75$ m. It is clear in this figure that, in the region above the slope, the fluid is cooler than the fluid in the deep region with a constant water depth.

At the early stage of the flow development, heat conduction through the water surface creates a thermal boundary layer under the surface, which is later broken by the instabilities in the form of sinking plumes (if the cooling is sufficiently strong). The present tests are concerned with the very early stage of the flow development in order to predict the onset time of the convective instabilities. As mentioned previously, the growth of the perturbations is well represented by the standard deviation of the temperatures taken at $y = -0.001$ m for $x > 1.0$ m, in which region the average fluid temperature is at the same level at a specific time. Fig. 2b shows the temperature responses to different amplitudes of the perturbation ($\varepsilon = 0.5\%$, 1.0%. 1.5%. 2.0%, 3.0%, and 4.0%) plotted on a logarithmic scale. Four distinct regions can be recognized in the time histories of the temperature standard derivation in this figure: a constant-response region, a transitional region in which the onset of instabilities can be recognized, an exponential-growth region (the linearly increasing section in the logarithmic plot), and a region following the exponential growth region with a peak in the growth curve. In fact, all these four regions belong to the initial flow development stage, which will be described (for the whole computational domain) later in this paper.

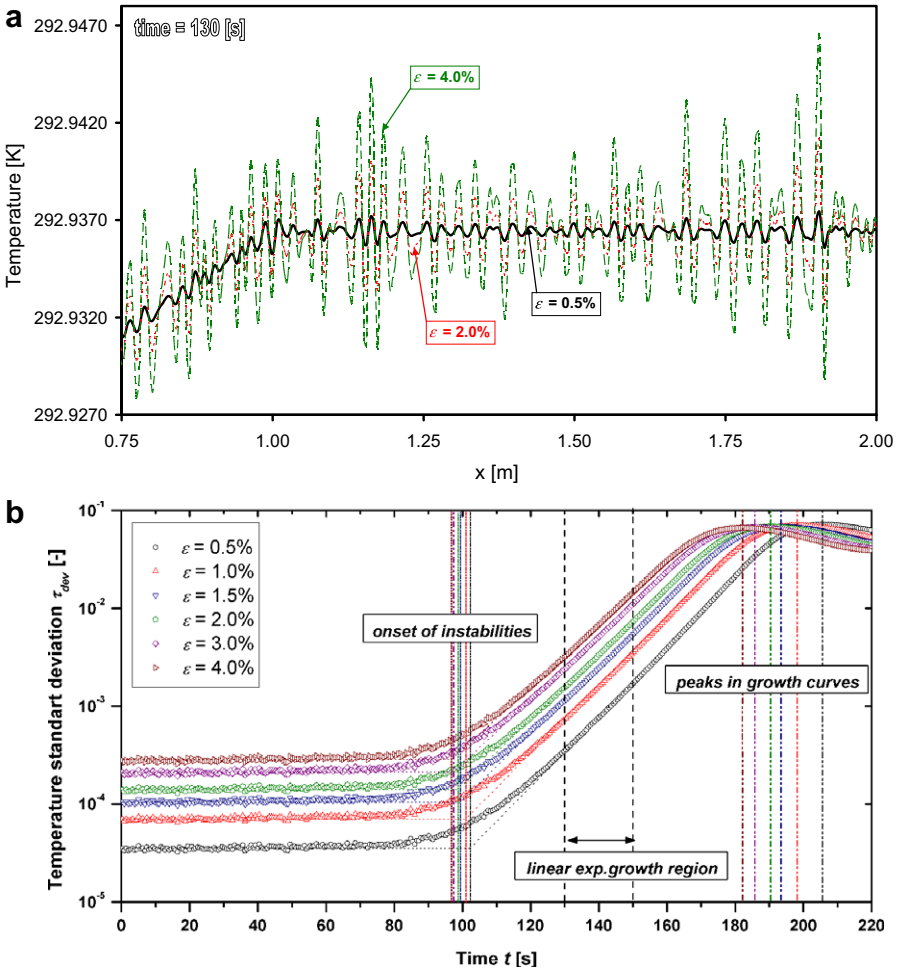

Fig. 2. Temperature responses to different perturbation amplitudes at $Pr = 7.07$ and $Gr = 10^7$. (a) The temperature profiles taken at $y = -0.001$ m at the time $t = 130$ s; (b) time series of the standard deviation of the temperature at $y = -0.001$ m and $x > 1.0$ m.

As seen in Fig. 2b, at the very early stage of cooling, the standard derivation of the temperature stays at a constant level. At this stage, the thermal boundary layer grows and remains stable. The low, but non-zero value of the standard deviation at this stage is an indication of the system response to the random perturbations. At a certain stage (around $t = 80$ s) the system response starts to increase, indicating the onset of instabilities. Between $t = 130$ and 150 s, the standard deviation of the temperature grows exponentially (represented by the straight lines in the logarithmic scale), which can be expressed by:

$$\tau_{dev} = a \exp\left[c(t - t_B)\right] \tag{11}$$

where a is the amplitude, c is the growth rate, and t_B is the critical time for the onset of instability. All these quantities can be determined from the time series of the temperature standard deviation shown in Fig. 2b. In the linear exponential growth region, the following relation is observed: if the amplitude of perturbation doubles, the temperature standard deviation τ_{dev} also increases by about two times at any specific time between $t = 130$ and 150 s.

The next region following the exponential growth region is characterized by the presence of a distinct peak on the growth curves. The peak occurs at the moment when the water directly below the surface becomes sufficiently dense so that sinking thermals are released locally from the thermal boundary layer. Fig. 2b shows that, the stronger the perturbations, the earlier the peak appear.

The onset time of the instabilities t_B is estimated as the time when the forward extended constant-response line meets the backward extended exponential growth line, as marked by the dotted lines in Fig. 2b. The computed numerical values of a, c, t_B, and τ_{dev} at $t = 130$ and 150 s are collected in Table 1. As seen, there is a slight variation of the growth rate, c, and the onset time of the instabilities, t_B, with the amplitude of the perturbation, and they both decrease with the increase of ε. The maximum variation of the growth rate is 3.81% for the parameters examined here. This variation is insignificant for the specified range of the amplitude of perturbations, and therefore the growth rate may be treated as a constant. Furthermore, the system responds in a linear way and the perturbation amplitudes do not change the stability properties (such as the onset time and growth rate) of the flow. Therefore, the applied perturbations have successfully triggered the instabilities without altering the basic properties of the flow.

4. Grid-dependency tests

A grid-dependency test was carried out to ensure the accuracy of the numerical solutions. The averaged volumetric flow rate Q_m was chosen for comparison purposes. Three different non-uniform meshes 431×26, 861×51 and 1281×76 were tested to check the dependence of the numerical solutions on the grid resolution at the highest Grashof number $Gr = 5 \times 10^7$ and $Pr = 7.07$. All cases gave similar results in terms of the flow response. Fig. 3 shows the

Table 1
Flow responses and the onset time of instabilities obtained with different perturbation strengths

ε	ε = 0.5%	ε = 1.0%	ε = 1.5%	ε = 2.0%	ε = 3.0%	ε = 4.0%
τ_{dev}, 130 s	3.50×10^{-4}	7.31×10^{-4}	1.13×10^{-3}	1.55×10^{-3}	2.39×10^{-3}	3.17×10^{-3}
τ_{dev}, 150 s	1.69×10^{-3}	3.49×10^{-3}	5.37×10^{-3}	7.26×10^{-3}	1.10×10^{-2}	1.44×10^{-2}
a	1.25×10^{-8}	2.77×10^{-8}	4.55×10^{-8}	6.62×10^{-8}	1.14×10^{-7}	1.66×10^{-7}
c	0.0787	0.0782	0.0778	0.0773	0.0765	0.0757
t_B	101.209	100.461	99.850	99.331	98.634	98.248

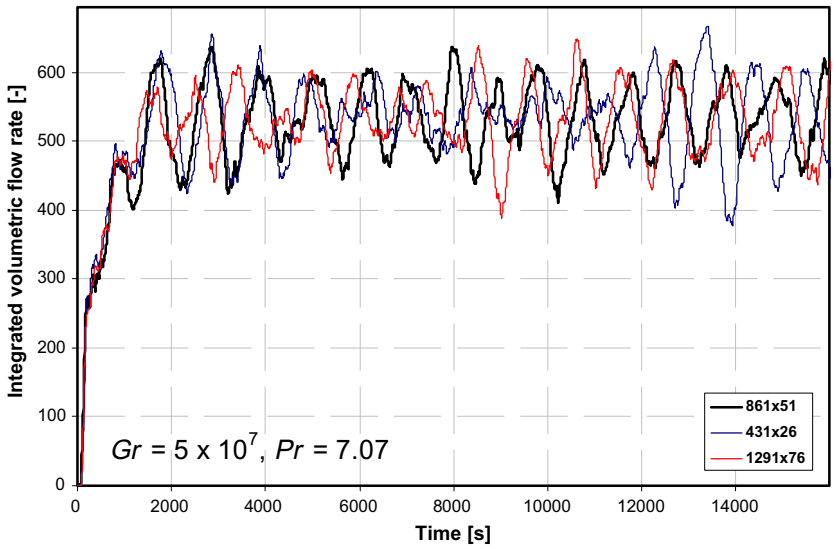

Fig. 3. Time histories of Q_m obtained for $Gr = 5 \times 10^7$ with three different meshes.

time histories of the averaged volumetric flow rates at $Gr = 5 \times 10^7$ obtained with the three meshes. Here, and in Fig. 11 to be presented later, the flow rate is normalized using the scale $\sim k$. The plot in Fig. 3 clearly shows that the overall flow development is comprised of three distinct stages, that is, an early stage with the volumetric flow rate increasing steadily, a transitional stage with the volumetric flow rate continuing to increase but subject to fluctuations, and a quasi-steady stage with the volumetric flow rate fluctuating about a constant mean value. It is seen that, at the very early stage, all the three solutions with different meshes are coincident. Subsequently, due to instabilities arising in the form of randomly distributed sinking plumes which are very sensitive to the grid resolution, the numerical solutions with different meshes start to diverge from each other during the transitional stage. However, the characters of the time series are very similar. Eventually, the flow becomes quasi-steady, which is evidenced by the oscillations of the averaged volumetric flow rate seen in Fig. 3. The flow in the quasi-steady stage retains almost the same structure over time, being only disturbed intermittently by the plunging thermals (refer to Section 5.3). The time-averaged volumetric flow rates at the quasi-steady state are compared in Table 2 for all three meshes tested. It is understood that the time-averaged quantity is very sensitive to the time period over which the volumetric flow rate is averaged, because even though the response is quasi-steady, there is some randomness in the occurrence of the plumes. This factor may have directly contributed to the relatively large variation of the solution with the finest mesh from the other two solutions. Nevertheless, the variation of the calculated time-averaged volumetric flow rate between the two fine meshes is less than 1.4% for $Gr = 5 \times 10^7$.

Table 2
Computed time-averaged integrated horizontal flow rate in the quasi-steady stage with different meshes

Mesh	Mesh size			Maximum variation
	431 × 26	861 × 51	1291 × 76	
Average, Q_m	537.64	535.28	528.08	1.78%

Table 3 gathers quantitative data of the stability properties obtained with the three different meshes at $Gr = 10^7$, for which random perturbations tests were carried out above. It is seen that the predicted values of the quantities vary from mesh to mesh. However, the maximum variation among the three meshes for the estimated quantities is only 2.42%. Therefore, based on the above-described mesh dependence tests and in consideration of the significant computing resources required with the finest mesh, the medium mesh of 861 × 51 is adopted for all subsequent computations. A time-step dependence test has also been carried out

Table 3
Results of the mesh-dependency test for $Gr = 10^7$ and $Pr = 7.07$

Mesh number: Mesh size:	1 431 × 26	2 861 × 51	3 1291 × 76	Maximum variation
Predicted time for the onset of instability	100.902	99.116	98.595	2.29%
Growth rate of the standard deviation	0.0765	0.0778	0.0784	2.42%

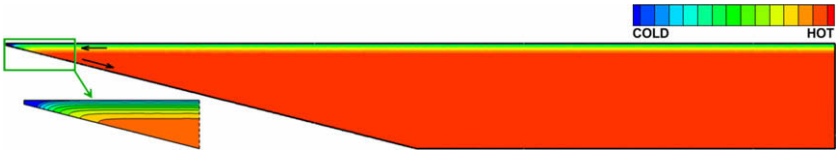

Fig. 4. Isotherms at the initial stage f the flow development (conductive effect, $Gr = 10^7$, $Pr = 7.01$, and $t = 120$ s). The dark arrows represent the direction of the convective circulation.

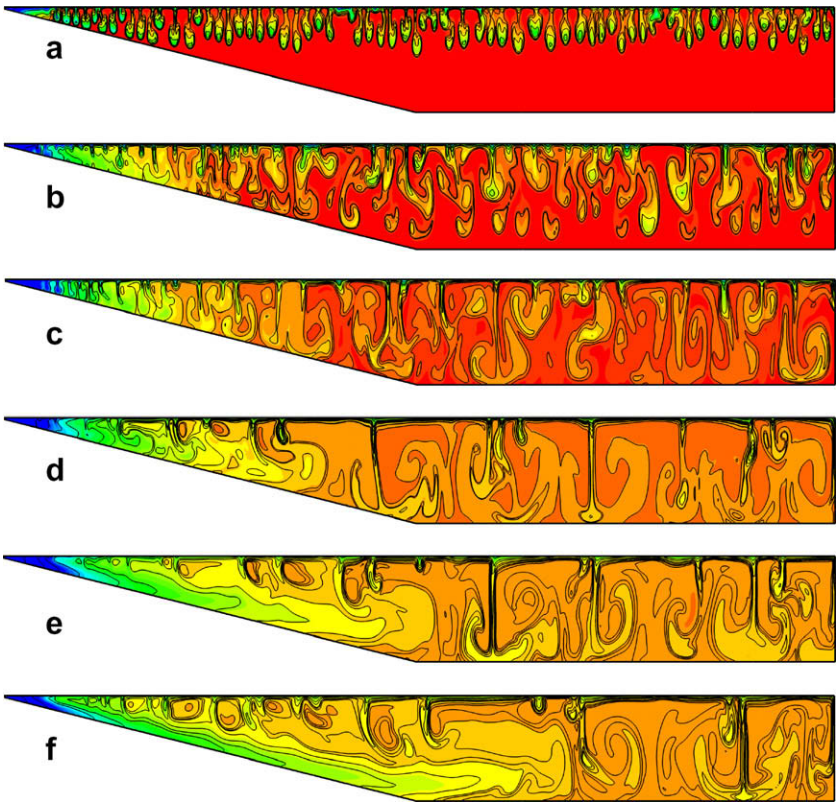

Fig. 5. Isotherms at the transitional stage for $Gr = 10^7$ and $Pr = 7.07$. (a) $t = 220$ s, (b) $t = 300$ s, (c) $t = 400$ s, (d) $t = 800$ s, (e) $t = 1200$ s, (f) $t = 1800$ s.

for the largest Grashof number, and an optimal time-step of 0.2 s is adopted for the present study.

5. Results and discussion

The random test presented above has revealed linearity of the flow response to varying perturbation amplitudes over the tested range. For all the subsequent numerical calculations, a fixed amplitude of perturbations $\varepsilon = 2.0\%$ is adopted. First, the transient flow development is described in detail for a fixed Grashof number $Gr = 10^7$. Numerical results for different Grashof numbers are then discussed. Finally, the present numerical data is compared with a previous scaling prediction of the onset time of instabilities.

5.1. Initial stage flow at 10^7

Initially, the water in the enclosure is isothermal. As soon as the surface cooling starts, the heat loss through the water surface results in a horizontal conductive boundary layer underneath the water surface, which is seen in Fig. 4. In this and all subsequent figures, blue[1] color always represents relatively cold regions and red color represents relatively warmer regions. Since we consider the general characteristics of the flow in reservoirs, the isotherms are always scaled in a way to demonstrate clearly the flow evolution at different Grashof numbers. It is seen in Fig. 4 that, in the shallow region, the isotherms curl over in order to satisfy the zero-flux boundary condition on the sloping bottom requiring that the isotherms become perpendicular to the slope. As a consequence, a temperature gradient is established along the sloping bottom, which is responsible for the generation of a convective flow with relatively colder water flowing down the slope into the deeper regions (the direction of the convective flow is denoted by the dark arrows in the figure). Since the surface heat flux is constant, the volumetric cooling rate decreases with increasing water depth, which results in a horizontal temperature gradient in the sloping region. The horizontal temperature gradient further reinforces the convective circulation.

5.2. Transitional stage flow at 10^7

Shortly after the initialization of the surface cooling, sinking cold-water plumes originating from the conductive surface layer can be observed (refer to Fig. 5a). These are due to cooling of the water body from above which results in the fluid near the surface becoming denser than that in the interior region. If the cooling is sufficiently strong, it leads to Rayleigh–Bernard type instabilities, and the thermals start to descend over the local water depth. The

[1] For interpretation of the references to colors in all figures, the reader is referred to the web version of this paper.

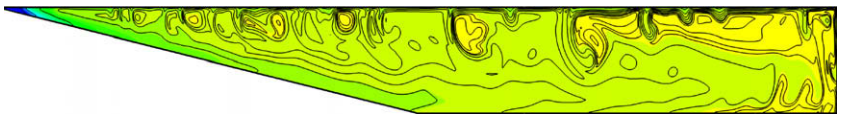

Fig. 6. Isotherms for $Gr = 10^7$ and $Pr = 7.07$ at $t = 8000$ s.

plunging thermals are responsible for the initial mixing of the fluid. The initial wave-number of the instabilities depends on the local rate of cooling. Those thermals located closer to the tip will reach the slopping bottom sooner, and through enhanced mixing, will accelerate the development of the convective circulation across the entire flow domain. As time increases, the plumes tend to merge, creating larger structures. Once these large flow structures of relatively cold water reach the bottom surface, they are prone to overturning, as seen in Fig. 5b and c. Sinking thermals in the shallow region cool that region quickly, and a cold undercurrent is created gradually above the slope as seen in Fig. 5d–f. The undercurrent slowly proceeds toward the deeper region, being constantly fed by a return flow of warm water along the surface.

As seen in Fig. 5e, the undercurrent reaches the end of the sloping region. At this moment it is possible to observe three distinct regions of the flow: the undercurrent on the sloping bottom, a surface return flow which is moving under the water surface toward the shallow end, and the deep region dominated by large sinking plumes. The thermals above the slope are becoming weaker and deformed by the undercurrent.

5.3. Quasi-steady stage flow at $Gr = 10^7$

Subsequently, the undercurrent reaches the vertical adiabatic end-wall, and the flow enters a quasi-steady state. At the quasi-steady state, the flow is fully developed and the averaged horizontal flow rate remains almost constant. The average temperature of the entire domain continues to decrease at this stage. Fig. 6 shows isotherms at the quasi-steady state ($t = 8000$ s). The relatively stable undercurrent is easily observed along the bottom. The return flow, unlike the undercurrent, is very unstable as the surface is being continuously cooled. Sinking plumes burst intermittently from the return flow below the water surface.

5.4. Temperature sampling at $Gr = 10^7$

Fig. 7 shows the temperature profiles $T(y)$ over the local water depth y at different horizontal locations $x = 0.03$, 0.04, 0.06, 0.085, 0.5, and 1.5 m and at $t = 100$ s which roughly corresponds to the estimated onset time of instabilities at $Gr = 10^7$ and $Pr = 7.07$ (refer to Section 3). An analytical solution for the conductive temperature profile relevant to the present boundary conditions is given in [19] as follows

$$T(y) = T_0 + 2\frac{H_0}{\lambda k}\left(\frac{kt}{\pi}\right)^{0.5}\exp\left(-\frac{y^2}{4kt}\right) + \frac{H_0}{\lambda k}\cdot y\cdot \mathrm{erfc}\left[\frac{y}{2(kt)^{0.5}}\right] \tag{12}$$

where λ is the thermal conductivity. The theoretical profile is marked on the plot with filled circles. The analytical solution agrees very well with the profile computed for the deep fluid region ($x = 1.5$ m). The same temperature profile is expected along different x positions where the local fluid depth is greater than the thickness of the thermal boundary layer (see for example $x = 0.5$ in Fig. 7). At this time, the water temperature at the surface in the deep region has dropped by about 0.2082 K with respect to its initial value T_0. This can be also confirmed by the theoretical prediction, calculated for $t = 100$ s and $y = 0$, using Eq. (12)

$$\Delta T(t) = -2\frac{H_0}{\lambda k}\left(\frac{kt}{\pi}\right)^{0.5} = 0.2083\ \mathrm{K} \tag{13}$$

The temperature profiles for $x = 0.5$ and 1.5 m in Fig. 7 suggest that the conduction boundary layer under the water surface has grown to a thickness of approximately 15 mm at 100 s. If a critical temperature difference relevant to the thickness of the conductive layer is reached, the surface layer will become unstable, and convective instabilities will initiate from the surface layer. For the thermal layer thickness of 15 mm, the critical temperature difference for the onset of Rayleigh–Benard type instabilities under the current flow configuration is estimated to be ~0.014 K, and thus the surface layer is in fact unstable at this time, as evidenced by the increased standard derivation of the surface temperature shown in Fig. 2(b). However those instabilities are still very weak at this time and thus are not discernible in the profiles in Fig. 7.

For a region close to the tip, the thermal boundary layer intersects the bottom and conduction dominates the heat transfer.

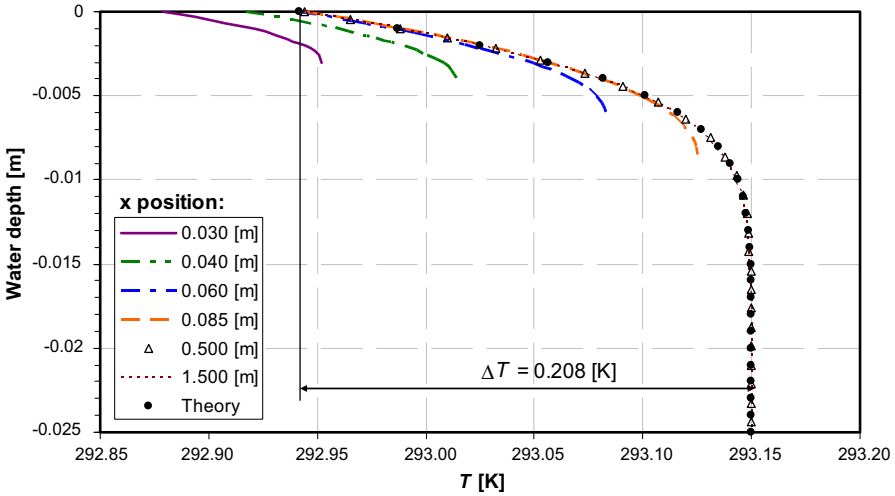

Fig. 7. Temperature profiles over the local water depth at different horizontal locations at $t = 100$ s.

As a consequence, the temperature difference between the surface and the bottom decreases towards the tip. Further, since the volumetric cooling rate is higher in the tip region, a positive horizontal temperature gradient is established in this region, as shown in Fig. 7.

Due to these mechanisms described above, two distinct regions will be created in the enclosure after the onset of convective instabilities ($t > t_B$): a conductive region close to the tip and a convective region in deeper areas. These are clearly seen in Fig. 5(a).

Fig. 8(a) shows the temperature time series at five different water depths ($y = 0.0$, -0.01, -0.02, -0.05, and -0.09 m) and at a fixed horizontal location $x = 1.0$ m for $Gr = 10^7$ and $Pr = 7.07$.

The temperature at the water surface reduces immediately after the surface cooling begins as expected, and initially follows the analytical solution for the temperature at $y = 0$ given by Eq. (13). At $y = -0.01$ m the temperature remains essentially at the initial value until around $t = 30$ s, at which time it also reduces significantly. This time series also follows the analytical solution at $y = -0.01$ m, given by Eq. (12). Similar behavior is observed for the deeper time series; with increasing depth, the time at which noticeable departure from the initial value is observed increases. For $y = 0$ and -0.01 m, the departure is clearly due to the growth of the thermal boundary layer from the cooling surface. That conclusion is not necessarily true for the deeper time series, as discussed below.

Around $t = 160$ s, the surface temperature time series shows a rapid increase in temperature. At the same time, the temperature at $y = -0.01$ m deviates from the analytical solution, also showing a small increase. These deviations occur at approximately the time when sinking cold-water plumes are released from the surface layer, and evidently the variations are due to the presence of the instabilities. In this case, discrete plunging plumes are carrying cold fluid from the surface, and the return flow is bringing relatively warm fluid to the surface. These are discrete events, and the x position at which these time series are taken is in the path of the return flow, and consequently a temperature rise is observed. However, the time series at the deeper locations are unaffected, and evidently the plumes at this time have not reached those deeper locations.

As time increases, the deeper locations deviate from their initial values. These deviations are much faster than would result from the pure conduction solution, and are the consequence of the presence of the instabilities. The response of an individual time series depends on the depth of the plunging plume affecting it or its location in the path of either a plunging cold plume or a warm return flow. For example, there is a clear indication of a plunging plume at

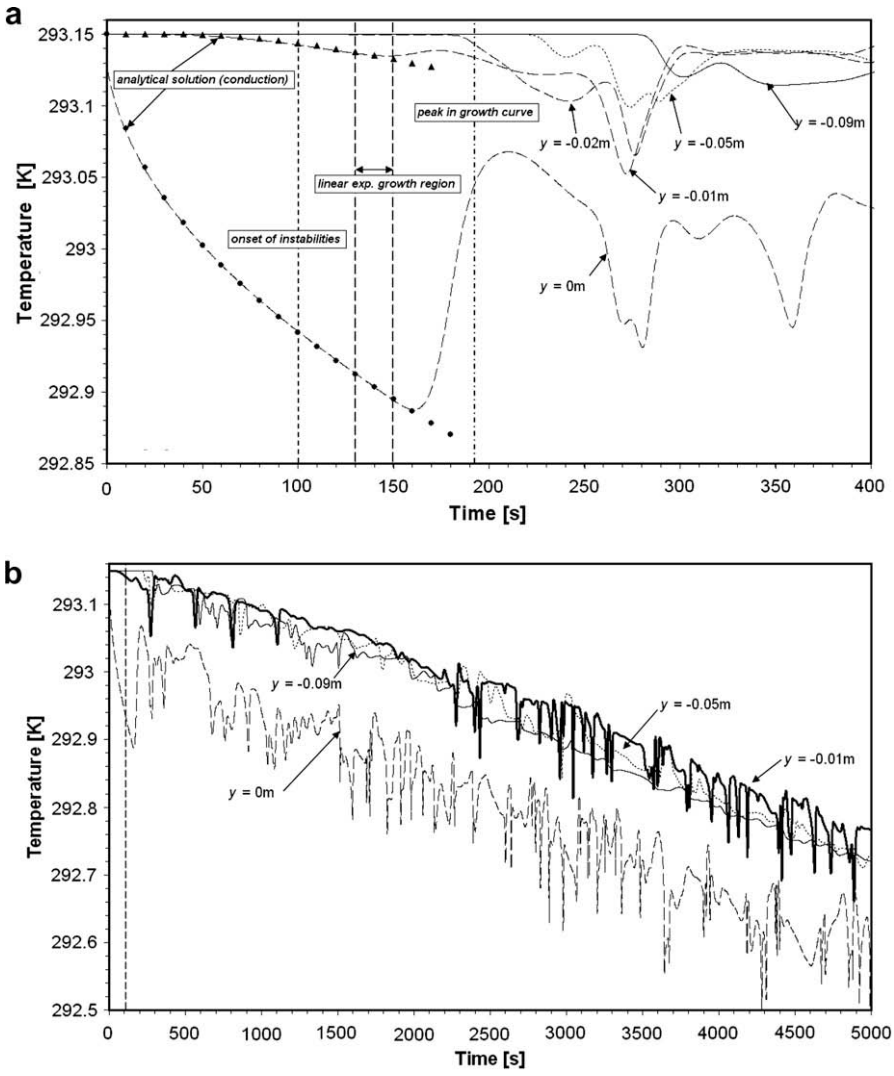

Fig. 8. Temperature time histories sampled at $x = 1.0$ m and at different water depths y for $Gr = 10^7$ and $Pr = 7.07$. (a) At the initial and early transitional stages and (b) over an extended period of flow development. The vertical dashed line indicates the time at which the instabilities start to occur.

approximately $t = 260$ s which affects all but the deepest location. At $t = 360$ s, a plume affects only the surface signal. Weaker indications of both plunging and rising fluid masses at other times are also present in the time series. The deviation of the temperature from the analytical solutions shown in Fig. 8(a) reinforces the conclusion that the presence of the instabilities is the dominant mechanism providing mixing.

Fig. 8(b) shows the temperature time series taken from the same locations but over a much longer period of the flow development. It can be seen in Fig. 8(b) that the overall temperature drops consistently with time despite fluctuations caused by the plunging thermals. The amplitude of the fluctuations due to the plumes decreases with increasing depth. It is also worth noting that the time-dependent temperatures in the deeper waters ($y = -0.01$, -0.05, and -0.09 m) are at approximately the same level, which is much higher than the temperature at the water surface ($y = 0$ m).

5.5. Dependence on the Grashof number

Fig. 9 shows isotherms in the transitional stage obtained for different Grashof numbers in order to demonstrate the variations of the characteristics of plunging thermals. It is clear that the transitional flow strongly depends on the Grashof number. As the Grashof number increases, the plunging thermals appear earlier, and they become smaller in size, indicating an increase of the wave number. It is also noticeable in Fig. 9 that a stable conductive region is present near the tip, and this stable region shrinks with increasing Grashof number.

Fig. 10 shows isotherms in the quasi-steady stage for four different Grashof numbers: $Gr = 10^4$, 10^5, 10^6, and 5×10^7, respectively. Although the times selected for presenting the data are different, the flows are all at comparable stages of development. Of particular interest is a comparison of the undercurrent and the surface return flow in each case. When the Grashof number is low ($Gr = 10^4$, Fig. 10a), the undercurrent is thick and stable. No instabilities in the form of unsteady sinking plumes are observed below the cooling surface. The undercurrent is also stable. At higher Grashof numbers ($Gr = 10^5$ and 10^6, Fig. 10b and c), the undercurrent is still relatively stable. However, the surface return flow is constantly disturbed by sinking plumes. The influence of the plumes on the undercurrent is relatively weak. For the highest Grashof number case ($Gr = 5 \times 10^7$) shown in Fig. 10(d), however, the undercurrent is noticeably disturbed by the thermals coming from the above, and the undercurrent separates from the bottom while interacting with the plumes. The flow maintains the general characteristics of having two main convective layers. The disturbances in the form of sinking plumes result in strong oscillatory

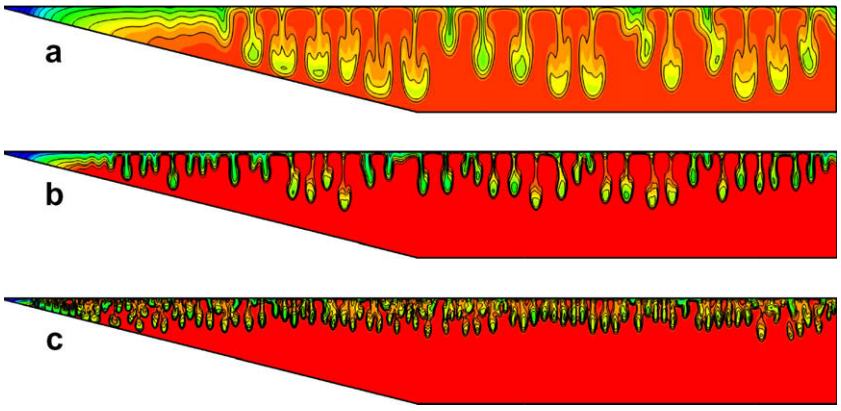

Fig. 9. Isotherms in the transitional state for $Pr = 7.07$. (a) $Gr = 10^5$, $t = 2400$ s; (b) $Gr = 10^6$, $t = 680$ s; (c) $Gr = 5 \times 10^7$, $t = 100$ s.

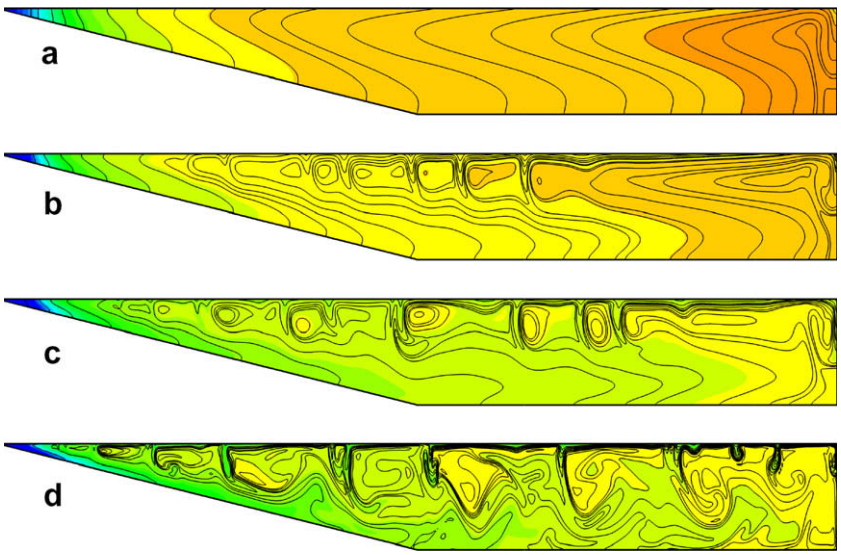

Fig. 10. Isotherms in the quasi-steady state for $Pr = 7.07$. (a) $Gr = 10^4$, $t = 143{,}360$ s; (b) $Gr = 10^5$, $t = 83{,}880$ s; (c) $Gr = 10^6$, $t = 20{,}000$ s; (d) $Gr = 5 \times 10^7$, $t = 4100$ s.

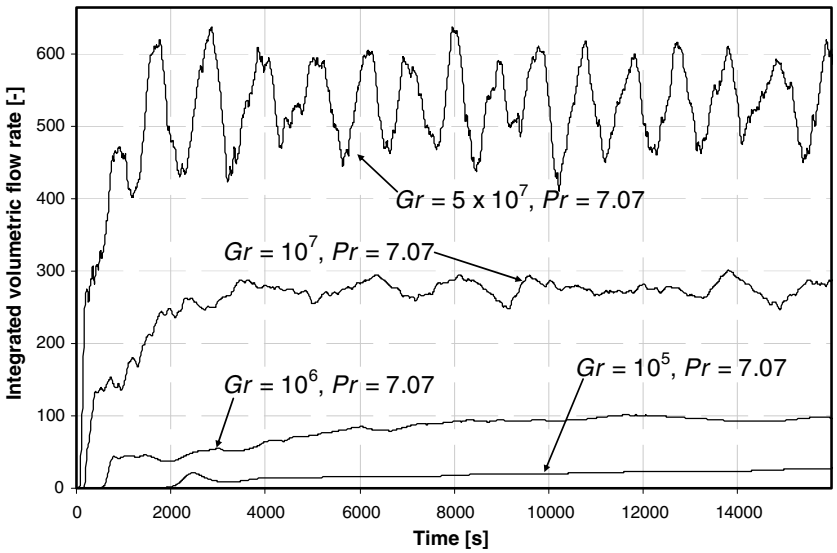

Fig. 11. Time series of the integrated volumetric flow rate for four different Grashof numbers.

behavior of the integrated volumetric flow rates, which are plotted in Fig. 11 for different Grashof numbers. Fig. 11 confirms that the flow is highly unstable for high Grashof numbers ($Gr = 10^7$ and 5×10^7) and relatively stable for lower Grashof numbers ($Gr = 10^5$ and 10^6). It is clearly seen in this figure that the intensity of the flow response increases with the Grashof number, that is, stronger cooling results in faster flow exchange. The three distinct stages of the flow development described previously, that is, an initial stage, a transitional stage and a quasi-steady stage can also be approximately identified in the plotted time series of the volumetric flow rate.

As mentioned above, the convective instabilities in the form of sinking cold-water plumes depend strongly on the Grashof number. The instabilities start earlier at higher Grashof numbers. The onset time of the instabilities can be estimated following the procedures outlined in [2,5]. According to [2,5], the stratification in the surface layer is potentially unstable and the instability sets in when the local Rayleigh number in the surface layer reaches a critical value of Ra_c. The local Rayleigh number is obtained as [2,5]:

$$Ra_L \sim \frac{g\beta H_0}{\nu k}\left(\frac{t}{k}\right)^{0.5}(kt)^{1.5} \sim Ra\left(\frac{tk}{h^2}\right)^2 \tag{14}$$

A comparison of the local Rayleigh number with the critical Rayleigh number yields a critical time scale for the onset of the instability at given Grashof and Prandtl numbers as:

$$t_B \sim \left(\frac{Ra_c}{Ra}\right)^{0.5}\frac{h^2}{k} \tag{15}$$

where $Ra_c \approx 657.5$ [2,20] for the present flow configuration. For $t < t_B$, the surface layer is stable, and for $t > t_B$, the instability will set in. The scale (15) indicates that the critical time for the onset of convective instability in the surface layer increases as the global Rayleigh number decreases. Fig. 12 plots the onset time of instability obtained using the method presented in Section 4.1 against the scaling prediction of (15). The plot clearly indicates a linear correlation between the predicted and actual onset times. Therefore, the time scale given by (15) is a good representation of the onset time of the convective instabilities.

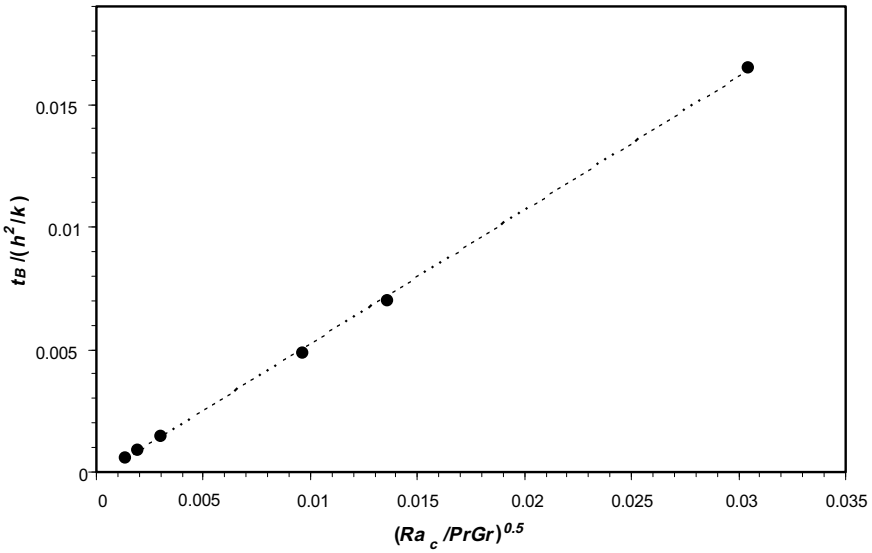

Fig. 12. Comparison of the estimated critical times with the predicted critical time of the scaling analysis.

6. Conclusions

The present work considers the night-time cooling of shallow waters with a gently sloping bottom. Initially, the water is isothermal and stationary in the numerical model. As soon as surface cooling starts, a conduction thermal boundary layer develops underneath the water surface. The thickness of the thermal layer increases with time while the temperature in the thermal boundary layer decreases with time. When the local Rayleigh number in the thermal boundary layer becomes sufficiently high, convective instabilities in the form of plunging plumes take place.

Numerical tests have been carried out to examine the flow response to random perturbations of different amplitudes (strengths). These revealed linearity of the flow response with an increase of the perturbation amplitude within the specified range. Following these tests, the transient flow development at different stages is described in detail, and the effects of the Grashof number on the flow and instability features are discussed. The present numerical results have demonstrated that two distinct thermal layers are formed in the resulting quasi-steady state flow at different Grashof numbers: an undercurrent along the bottom and an unstable return flow immediately under the water surface. Further, the heat transfer in the tip region is primarily by conduction, with a corresponding relatively simple flow, whereas in the deeper region instabilities dominate the flow if the Grashof number is sufficiently large. In this region, the primary mode of heat transfer is vertical convection by the resulting plumes. It was also shown that stability of the undercurrent and return flow strongly depends on the Grashof number.

The unsteady flow structures obtained in the present numerical simulations have also been observed in our recent experiments carried out in a reservoir model cooled from above [6], where the development of an unsteady convection was described based on experimental flow visualization and quantitative temperature measurements with thermo-chromic liquid crystals. Although direct comparisons are not possible since the boundary conditions for the experiment and numerical cases were different, general comparisons may be made. The experimental results have confirmed the general behavior of the flow development under night-time cooling conditions which are described in this paper. The flow visualization of the experiment revealed three stages of the flow development: the growth of a horizontal thermal boundary layer under the water surface, the initiation of convective instabilities, and further development of the flow with the formation of an undercurrent and a surface return flow.

Additionally, both the experimental and numerical results indicate that the convective motions in reservoirs induced by night-time cooling are very important from environmental and ecological points of view. Water circulation driven by horizontal thermal gradients, as presented above, may cause the transport of small suspended pollutants or biological particles or dissolved constituents into or from deep-water regions and thus play a significant role in determining water quality. The present paper however, considers only convective motions of the water, and a further study of particle transport, which is beyond the scope of the present investigation, will help to understand how the relative phase and motions of particles may be calculated and applied to ecological transport models.

Acknowledgement

The authors gratefully acknowledge the financial support of the Australian Research Council.

References

[1] J. Imberger, J.C. Patterson, Physical limnology, Adv. Appl. Mech. 27 (1990) 303–475.
[2] C. Lei, J.C. Patterson, Unsteady natural convection in a triangular enclosure induced by surface cooling, Int. J. Heat Fluid Flow 26 (2005) 307–321.
[3] C. Lei, J.C. Patterson, A direct stability analysis of a radiation-induced natural convection boundary layer in a shallow water, J. Fluid Mech. 480 (2003) 161–184.
[4] C. Lei, J.C. Patterson, A direct three dimensional simulation of radiation-induced natural convection in a shallow wedge, Int. J. Heat Mass Transfer 46 (2003) 1183–1197.
[5] C. Lei, J.C. Patterson, Unsteady natural convection in a triangular enclosure induced by absorption of radiation, J. Fluid Mech. 460 (2002) 181–209.
[6] T.P. Bednarz, C. Lei, J.C. Patterson, An experimental study of unsteady natural convection in a reservoir model cooled from the water surface, Exp. Therm. Fluid Sci. 32 (2008) 844–856.
[7] G.M. Horsch, H.G. Stefan, Convective circulation in littoral water due to surface cooling, Limnol. Oceanogr. 33 (5) (1988) 1068–1083.
[8] G.M. Horsch, H.G. Stefan, S. Gavali, Numerical simulation of cooling-induced convective currents on a littoral slope, Int. J. Numer. Methods Fluids 19 (1994) 105–134.
[9] E.E. Adams, S.A. Wells, Field measurements on side arms of Lake Anna Va, J. Hydraulic Eng. 110 (1984) 773–793.
[10] S.G. Monismith, J. Imberger, M.L. Morison, Convective motions in the sidearm of a small reservoir, Limnol. Oceanogr. 35 (1990) 1676–1702.
[11] C. Lei, J.C. Patterson, Natural convection induced by diurnal heating and cooling in a reservoir with slowly varying topography, JSME Int. J. Ser. B – Fluids Therm. Eng. 49 (3) (2006) 605–615.
[12] D.E. Farrow, J.C. Patterson, On the response of a reservoir sidearm to diurnal heating and cooling, J. Fluid Mech. 246 (1993) 143–161.
[13] D.E. Farrow, Periodically forced natural convection over slowly varying topography, J. Fluid Mech. 508 (2004) 1–21.
[14] W.H. Press, S.A. Teukolsky, W.T. Vetterling, B.P. Flannery, Numerical Recipes in C++: The Art of Scientific Computing, Cambridge University Press, Cambridge, MA, 2002, ISBN 0-521-75033-4.
[15] S.V. Patankar, Numerical Heat Transfer and Fluid Flow, Hemisphere, NY, 1980, ISBN 0-891-16522-3.
[16] H.K. Versteeg, W. Malalasekera, An Introduction to Computational Fluid Dynamics: The Finite Volume Method, Addison Wesley Longman, Reading, MA, 1995, ISBN 0-582-21884-5.
[17] S. Armfield, R. Janssen, A direct boundary-layer stability analysis of steady-state cavity convection flow, Int. J. Heat Fluid Flow 17 (1996) 539–546.
[18] R. Janssen, S. Armfield, Stability properties of the vertical boundary layers in differentially heated cavities, Int. J. Heat Fluid Flow 17 (1996) 547–556.
[19] A. Bejan, Heat Transfer, John Wiley and Sons Inc., New York, 1993, ISBN 0-471-50290-1.
[20] P.G. Drazin, Introduction to Hydrodynamic Stability, Cambridge University Press, Cambridge, MA, 2002, ISBN 0-521-00965-0.